

Design and Analysis of Permanent Magnet Motor with Movable Stators

Chun-Chi Lai¹, Tzong-Shi Liu^{1, *}, and Ming-Tsan Peng²

Abstract—Permanent-magnet motors are widely used in-wheel motors of electric vehicles and hybrid vehicles. Based on a movable stator design, this paper presents a new type permanent-magnet motor, whose torque can be adjusted in order to meet different driving requirements. The stator geometry is varied by means of changing movable stator positions. Accordingly, the air-gap length in permanent-magnet motors is changed so that torque can be adjusted. To derive an analytical model, Fourier series expansions are employed to formulate air-gap geometry variation. The analytical model is validated by finite element numerical results. Concerning motor torque variation capability achieved in this study, the ratio of the largest vs. the smallest torque is 2.3.

1. INTRODUCTION

A desirable feature of permanent-magnet (PM) motors is high torque at low speed, and therefore suitable as a direct-drive actuator in electric vehicles (EV) or hybrid vehicles. The high torque feature helps acceleration performance of EV. Vernier machines [1, 2] belong to PM motors and are adequate as an in-wheel motors. High torque and high efficiency feature are caused by a magnetic gearing effect. Toothed-pole structures play an important role in torque-maximizing design of vernier machines. To increase torque, dual-excitation permanent magnet vernier machines [3] including inner-stator and outer-stator were presented.

The same motor volume that can generate larger torque will gain advantage in EV performance. Both increases of armature magnetomotive force and inner diameter of stator are approaches to raising torque performance with the same machine volume [4]. Different stator shapes and magnet configurations will cause different flux densities and torque performances, respectively. A relationship between the stator shape and flux density was developed in order to predict motor performance [5]. A finite element method was used to analyze the electromagnetic torque of PM machines with concentrated winding, whose results show that the torque is affected by magnetic saturation [6].

Smaller air gap improves the motor torque, but there is still a mechanical limitation on the length of air gap. Hence, 3-D air gaps were proposed [7] to improve motor torque without increasing the amount of rare earth materials. The result shows that 3-D air-gap performance is equivalent to the improvement of 70% shortened gap. The effects of slot geometric details are difficult to evaluate by analytical methods only. A method, which combines analytical with numerical computation, called semi-analytical method [8] was thus proposed.

A genetic-algorithm loop was used to optimize the lamination design and verified with finite element analysis [9]. Magnetic gears were integrated into permanent-magnet brushless DC motors in order to achieve both high efficiency and high power density [10]. A direct drive motor with rare earth magnets that forms the outside of the motor was designed by using finite element electromagnetic

Received 15 December 2013, Accepted 18 February 2014, Scheduled 26 February 2014

* Corresponding author: Tzong-Shi Liu (tsliu@mail.nctu.edu.tw).

¹ Department of Mechanical Engineering, National Chiao Tung University, Hsinchu 30010, Taiwan. ² Industrial Technology Research Institute, Hsinchu 31040, Taiwan.

field analysis [11]. A modular flux-switching permanent-magnet motor was analyzed and compared with fault-tolerant motors [12]. Both simplified and exact analytical models [13] were applied to predict magnetic field distribution and electromagnetic performances of parallel double excitation and spoke-type permanent magnet motors. An axial-flux permanent-magnet brushless DC motor [14] was optimized by carrying out finite element analysis and genetic algorithm. In this study, the permanent magnet motor with movable stators has been proposed. The torque variation capability can be achieved by means of changing movable stators positions. The Fourier series expansions are employed in analytical model to formulate air-gap geometry variation. The analytical model is used to analyze and validate by finite element numerical results. The performance of the proposed motor including flux density, cogging torque and back-EMF are simulated and analyzed.

2. MATHEMATICAL MODEL OF PMVM WITH MOVABLE STATOR

The flux density equation of PM motors with movable stator can be obtained by analyzing permeance coefficients and air gaps. The 3D construction of stator with movable stators is shown in Figure 1(a), and the exploded diagram is shown in Figure 1(b). As shown in Figure 1(b), the white part is movable stator holder which can be made by nonmagnetic materials. The movable stator holder connects to the movable stators. Hence, movable stators rotate along the same axle as the motor shaft. The red parts are movable stators and gray part is fixed stator and both parts can be made by silicon steel. Figure 2 shows the 2D construction of a PM motor, which belongs to an outer rotor type, with a fixed stator and nine movable stators. The fixed stator consists of nine long teeth and nine short teeth. As depicted in Figure 2, R_s denotes the stator radius of the nine long teeth. The number 9 of movable stators is intended to equal half the number 18 of slots so that all of teeth profile and length become the same when nine movable stators are moved to the position of short stator teeth. The winding configuration belongs to the concentrated type in a slot. The fixed stator of eighteen teeth and nine movable stators are all made of silicon steel. To shift positions of the movable stators that can be rotated along the same axis as the motor shaft, a motor or gears may be used.

The winding pattern in this study is shown in Figure 3. The winding connection generates 6 poles in the fixed stator, and the winding is concentrated type. In addition, the winding is designed for three-phase permanent magnet motor. Hence, the winding is provided with six terminals including three input and three output terminals.

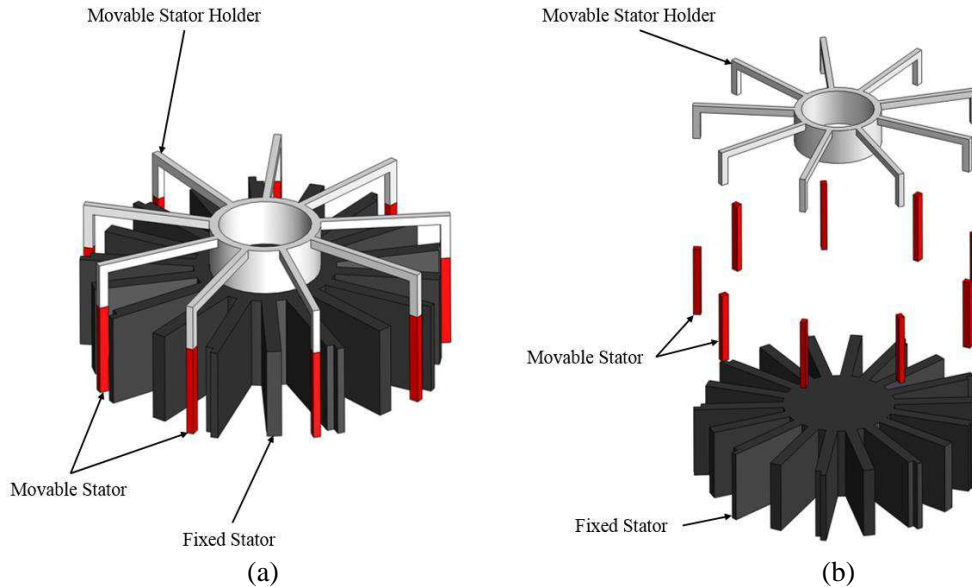


Figure 1. (a) 3D diagram of PM motor with nine movable stators, movable stator holder and one fixed stator. (b) Exploded diagram.

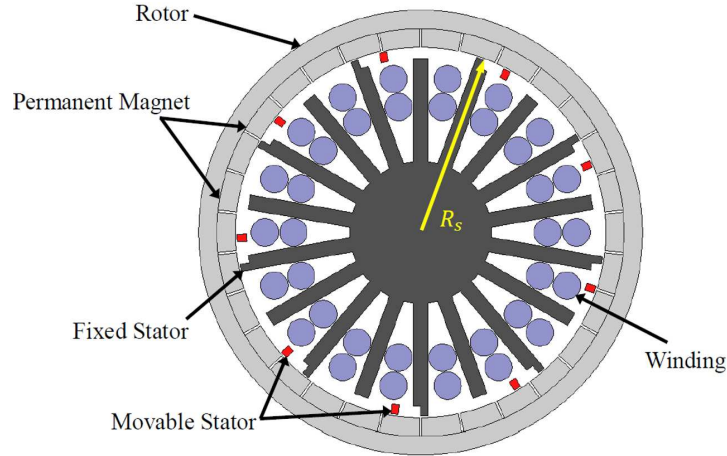


Figure 2. 2D diagram of PM motor with nine movable stators and one fixed stator.



Figure 3. Winding pattern for three-phase 18-slot motor.

Magnitudes of the magnetomotive force, flux density and permeance coefficient all depend on the air gap that is related to the stator geometry. The permeance coefficient is expressed by [12]

$$\lambda(\theta_m) = \frac{\mu_0}{\delta(\theta_m)} \tag{1}$$

where θ_m , μ_0 and $\delta(\theta_m)$ denote the mechanical angle, permeability and air gap length, respectively. Hence, the air-gap permeance coefficient is inversely proportional to $\delta(\theta_m)$.

2.1. Permeance Coefficient of Stator with Movable Stators

The air-gap length under movable stator is much shorter than a pole-pitch in practical machines. Therefore, magnetic flux can be treated as passing through air gap in radial direction. Figure 4 depicts the schematic of a stator tooth, in which the red part is a movable stator, and the gray part is a stator tooth. The widths of the movable stator and stator tooth are W_m and W_t , respectively. The permeance coefficient $\lambda(\theta_m)$ inversely varies with the air gap $\delta(\theta_m)$. The air-gap $\delta(\theta_m)$ between permanent magnet and movable stator does not vary when W_t is much smaller than W_m or $W_t = 0$. Hence, the calculation of permeance coefficient $\lambda(\theta_m)$ is established even if W_t is much smaller than W_m or $W_t = 0$. Accordingly, Figure 5 depicts air gaps between the rotor and movable stator. Figure 5(b) shows the equivalent stator geometry of Figure 5(a) for the ease of calculation.

Figure 5 depicts stator geometry $f_s(\theta_m)$ vs. mechanical angle θ_m . In Figure 5, gray parts represent the fixed stator, and red parts represent movable stators. The air gap is the distance between the permanent magnet rotor and the stators. The horizontal axis represents the angle due to movable stator rotation. In addition, R denotes the height between the PM rotor and the stator base, and d denotes the angle along a stator tooth width. The stator tooth width denotes the product of R_s and

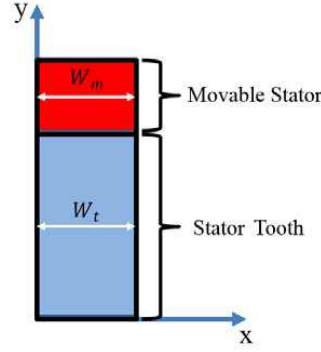


Figure 4. Schematic of a stator tooth that consists of a movable stator with width W_m and a tooth with width W_t .

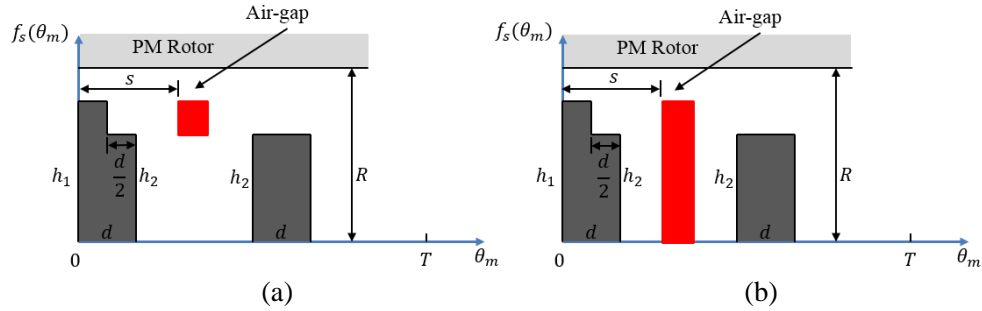


Figure 5. (a) Schematic of stator geometry with movable stator. (b) Schematic of equivalent stator geometry. The gray parts are the fixed stator, the red part is the movable stator, and the air gap is the distance between the permanent magnet rotor and the stators. The horizontal axis represents the angle due to movable stator rotation.

d , s denotes the angle from to the movable stator, h_1 denotes the stator tooth height, h_2 , denotes the height between movable stator and stator base, and T denotes the periodic angle of stator geometry. According to Figure 5, the air gap dimension can be expressed by

$$\delta(\theta_m) = R - f_s(\theta_m) \quad (2)$$

The current study expresses air-gap geometry in terms of Fourier series expansion. Accordingly, the stator geometry $f_s(\theta_m)$ of the presented stator design incorporating movable stators is expressed by

$$f_s(\theta_m) = f_a(\theta_m) + f_b(\theta_m) + f_c(\theta_m) \quad (3)$$

where $f_a(\theta_m)$, $f_b(\theta_m)$, and $f_c(\theta_m)$ are square waves respectively represented by Fourier series

$$f_a(\theta_m) = \frac{h_2 d}{2T} + \sum_{n=1}^{\infty} \frac{2h_2}{n\pi} \sin \frac{n\pi d}{2T} \cos \left(\frac{n\pi(\theta_m - \frac{d}{2})}{T} \right) \quad (4)$$

$$f_b(\theta_m) = \frac{(h_1 - h_2)d}{4T} + \sum_{n=1}^{\infty} \frac{2(h_1 - h_2)}{n\pi} \sin \frac{n\pi d}{4T} \cos \left(\frac{n\pi(\theta_m - \frac{d}{4})}{T} \right) \quad (5)$$

$$f_c(\theta_m) = \frac{h_1 d}{4T} + \sum_{n=1}^{\infty} \frac{2h_1}{n\pi} \sin \frac{n\pi d}{4T} \cos \left(\frac{n\pi(\theta_m - (s + \frac{d}{4}))}{T} \right) \quad (6)$$

Figure 6 shows that the movable stator can be moved a certain angle in the stator slot. For example, the movable stator can be moved $s_1 - \frac{d}{2}$ angle or $s_2 - \frac{d}{2}$ angle, as shown in Figures 6(b) and 6(c), respectively. Moreover, the geometric period in Figure 6(a) is twice as long as the geometric period in 6(d).

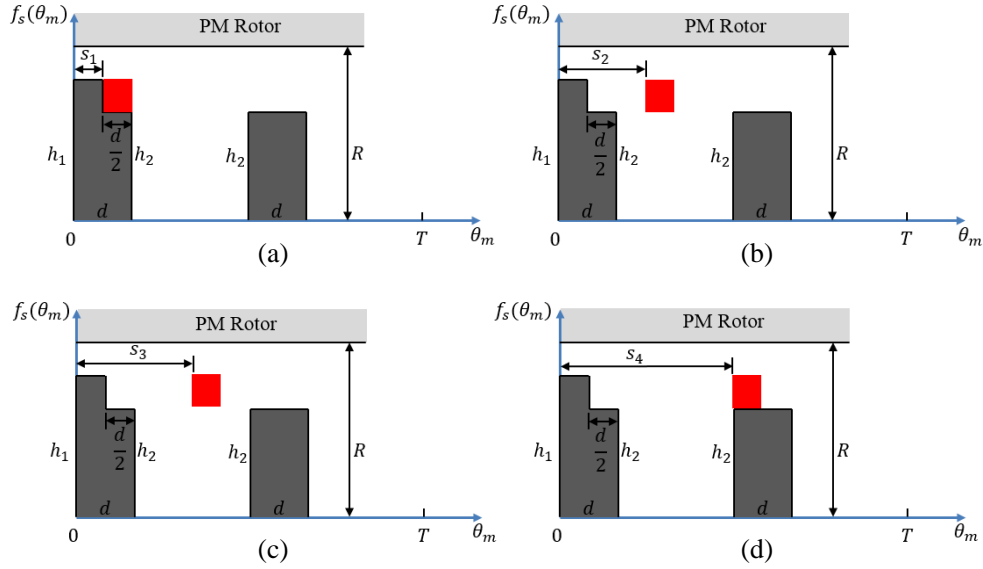


Figure 6. (a) The leftmost position of movable stator. (b) The first intermediate position of movable stator. (c) The second intermediate position of movable stator. (d) The rightmost position of movable stator.

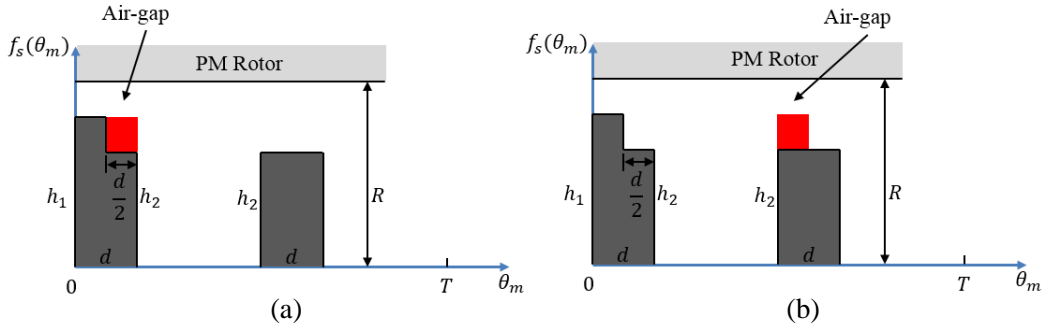


Figure 7. (a) Schematic of air gap when the movable stator is moved to touch the left-side fixed stator tooth. (b) Schematic of air gap when the movable stator is moved to touch the right-side fixed stator tooth.

The movable stator can touch either the left or right fixed stator tooth, shown in Figure 7. The air gap is formed between stator tooth and permanent magnet when the movable stator is moved to touch the left-side fixed stator tooth depicted in Figure 7(a). On the other hand, the air gap is formed between the eighteen teeth of the fixed stator and thirty permanent magnets when the movable stator is moved to touch the right-side fixed stator tooth shown in Figure 7(b).

As shown in Figure 7(a), the stator geometry $f_s(\theta_m)$ with the movable stator integrated into the left-side fixed stator tooth that is the sum of square waves $f_{La}(\theta_m)$ and $f_{Lb}(\theta_m)$ can be expressed by

$$f_s(\theta_m) = f_{La}(\theta_m) + f_{Lb}(\theta_m) \tag{7}$$

where $f_{La}(\theta_m)$ and $f_{Lb}(\theta_m)$ are square waves respectively represented by Fourier series

$$f_{La}(\theta_m) = \frac{h_2 d}{2T} + \sum_{n=1}^{\infty} \frac{2h_2}{n\pi} \sin \frac{n\pi d}{2T} \cos \left(\frac{n\pi (\theta_m - \frac{d}{2})}{T} \right) \tag{8}$$

$$f_{Lb}(\theta_m) = \frac{(h_1 - h_2)d}{2T} + \sum_{n=1}^{\infty} \frac{2(h_1 - h_2)}{n\pi} \sin \frac{n\pi d}{2T} \cos \left(\frac{n\pi (\theta_m - \frac{d}{2})}{T} \right) \tag{9}$$

As shown in Figure 7(b), the stator geometry $f_s(\theta_m)$ with the movable stator integrated into the right-side fixed stator tooth can be expressed by

$$f_s(\theta_m) = f_{Ra}(\theta_m) + f_{Rb}(\theta_m) \quad (10)$$

where $f_{Ra}(\theta_m)$ and $f_{Rb}(\theta_m)$ are square waves respectively represented by Fourier series

$$f_{Ra}(\theta_m) = \frac{h_2 d}{2T} + \sum_{n=1}^{\infty} \frac{2h_2}{n\pi} \sin \frac{n\pi d}{2T} \cos \left(\frac{n\pi(\theta_m - \frac{d}{2})}{T} \right) \quad (11)$$

$$f_{Rb}(\theta_m) = \frac{(h_1 - h_2)d}{2T} + \sum_{n=1}^{\infty} \frac{2(h_1 - h_2)}{n\pi} \sin \frac{n\pi d}{4T} \cos \left(\frac{n\pi(\theta_m - \frac{d}{4})}{T} \right) \quad (12)$$

The stator model with the movable stators has been obtained based on Fourier series expansion. Depending on movable stator positions, there exist three sets of formulation. The stator geometry is a periodic square wave composed of (4), (5), and (6) when the movable stators are located off the fixed stators on the left and right sides. In a similar manner, the stator geometry is a periodic square wave composed of (7), (8), and (9) when the movable stators are integrated into the left side of the fixed stator. By contrast, if the movable stators are integrated into the right side of the fixed stator, the stator geometry is a periodic square wave composed of (10), (11), and (12).

2.2. Rotor Magnetomotive Force

The fundamental component of the magnetomotive force produced by permanent magnets is expressed as [4]

$$F_M = F_{SM} \cos(Z_1 \theta_m) + F_{RM} \cos(Z_2 \theta_{rm}) \quad (13)$$

where F_{SM} and F_{RM} denote the magnetomotive force of the stator and the rotor, respectively. In general, the stator is made of steel. Permanent magnets belong to a part of the rotor. Thus, the rotor magnetomotive force can be expressed by

$$F_{RM}(\theta_{rm}) = \sum_{n:\text{odd}}^{\infty} \frac{F_{RM1}}{n} \cos(nZ_2 \theta_{rm}) \quad (14)$$

where F_{RM1} denotes the amplitude of the fundamental component, Z_2 the pole pair number of the rotor, θ_m the mechanical angle, θ_{rm} the mechanical angle on the rotor, and θ_r the rotor position.

According to Figure 8, the mechanical angle on the rotor is written as

$$\theta_{rm} = \theta_m - \theta_r \quad (15)$$

Substituting (15) into (14) yields

$$F_{RM}(\theta_m) = \sum_{n:\text{odd}}^{\infty} \frac{F_{RM1}}{n} \cos\{nZ_2(\theta_m - \theta_r)\} \quad (16)$$

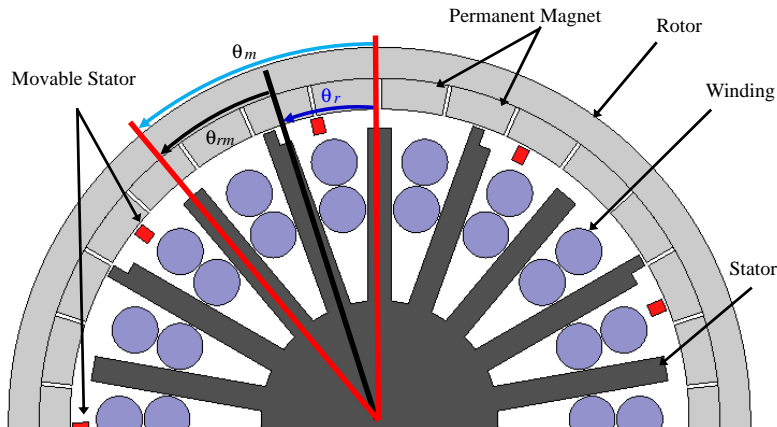


Figure 8. Relationship among mechanical angle θ_m , rotor mechanical angle θ_{rm} , and rotor position θ_r .

Therefore, the rotor magnetomotive force can be calculated by using (16) where Z_2 denotes the pole pair number in the rotor.

2.3. Flux Density

The flux density in the air gap is generated by PM. Since flux density B_{PM} equals the product of the PM magnetomotive force and permeance coefficient [15],

$$B_{PM} = F_{RM} \lambda(\theta_m) \tag{17}$$

Substituting (1) and (2) into (17) gives

$$B_{PM} = F_{RM} \frac{\mu_0}{\delta(\theta_m)} = F_{RM} \frac{\mu_0}{R - f_s(\theta_m)} \tag{18}$$

Substituting (16) into (18) yields

$$B_{PM} = \sum_{n:odd}^{\infty} \frac{F_{RM1}}{n} \cos \{nZ_2(\theta_m - \theta_r)\} \frac{\mu_0}{R - f_s(\theta_m)} \tag{19}$$

Derived in this study, B_{PM} is the analytical form of the flux density generated by permanent magnets in the rotor.

2.4. Stator Magnetomotive Force

Assume that the present motor contains a three phase winding and that the winding is driven by a three-phase balanced supply. In each phase, the stator magnetomotive force shown in Figure 9 is generated by the balanced supply.

According to Figure 9, the stator magnetomotive force can be modeled by using the Fourier series expansion that is expressed by

$$F_c(\theta_e) = \sum_{n=1}^{\infty} a_n \sin n\theta_e \tag{20}$$

where θ_e denotes the electrical angle and

$$a_n = \frac{4P}{\pi} \int_0^{\frac{\pi}{2P}} F_c(\theta_e) \sin n\theta_e d\theta_e \tag{21}$$

Substituting (21) into (20) yields

$$F_c(\theta_e) = \sum_{n=1}^{\infty} \frac{4}{n\pi} \frac{NI}{2p} \sin n\theta_e \tag{22}$$

which represents the single-phase stator magnetomotive force.

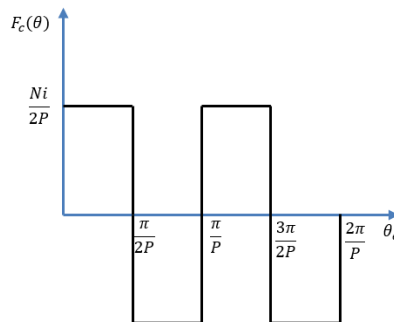


Figure 9. Air-gap magnetomotive force.

The current of a balanced 3-phase supply can be written as

$$\begin{aligned} I_U &= I \cos \omega t \\ I_V &= I \cos \left(\omega t - \frac{2\pi}{3} \right) \\ I_W &= I \cos \left(\omega t + \frac{2\pi}{3} \right) \end{aligned} \quad (23)$$

The magnetomotive force of phase U can be expressed by

$$F_U = \frac{1}{2} (F_c \sin(\theta_e - \omega t) + F_c \sin(\theta_e + \omega t)) \quad (24)$$

Similarly, for phases V and W , one has

$$F_V = \frac{1}{2} \left(F_c \sin(\theta_e - \omega t) + F_c \sin \left(\theta_e + \omega t - \frac{2\pi}{3} \right) \right) \quad (25)$$

$$F_W = \frac{1}{2} \left(F_c \sin(\theta_e - \omega t) + F_c \sin \left(\theta_e + \omega t + \frac{2\pi}{3} \right) \right) \quad (26)$$

Summing (24), (25), and (26) yields the total magnetomotive force

$$F(\theta_e, t) = F_U + F_V + F_W \quad (27)$$

Based on (22) and (27),

$$F(\theta_e, t) = \frac{3}{2} F_c \sin(\theta_e - \omega t) = F_{3ph} \sin(\theta_e - \omega t) \quad (28)$$

where F_{3ph} denotes a stator magnetomotive force generated by 3-phase full-pitch concentrated winding. (28) gives

$$F_{3ph} = \frac{3}{2} F_c \quad (29)$$

Substituting (22) into (29) leads to

$$F_{3ph}(\theta_e) = \sum_{n=1}^{\infty} \frac{3}{2} \frac{4}{n\pi} \frac{NI}{2P} \sin(n\theta_e \mp \omega t) \quad (30)$$

where

- sign holds for $n = 1, 7, 13, \dots$
- + sign holds for $n = 5, 11, 17, \dots$
- All other terms are zero

and I denotes the current, N the number of turns, P the number of pole-pairs, ω the rotor angular velocity, and θ_e the electrical angle.

The mechanical angle θ_m is related to the electrical angle θ_e by [16]

$$\theta_e = P\theta_m \quad (31)$$

Substituting (31) into (30) gives

$$F_{3ph}(\theta_m) = \sum_{n=1}^{\infty} \frac{3}{2} \frac{4}{n\pi} \frac{NI}{2P} \sin(nP\theta_m \mp \omega t) \quad (32)$$

where

- sign holds for $n = 1, 7, 13, \dots$
- + sign holds for $n = 5, 11, 17, \dots$
- All other terms are zero

A winding factor k_w that accounts for departure from concentrated full-pitch windings [16] can be expressed by

$$k_w = k_{pn}k_{dn} \quad (33)$$

where

$$k_{pn} = \sin \frac{n\alpha}{2} \quad (34)$$

is a pitch factor and

$$k_{dn} = \frac{\sin \frac{nm\gamma}{2}}{m \sin \frac{n\gamma}{2}} \quad (35)$$

is a distribution factor. α denotes the coil pitch, γ the electrical angle between adjacent windings, and m the number of windings. Incorporating the winding factor k_w into (32) results in

$$F_{3ph}(\theta_m) = \sum_{n=1}^{\infty} \frac{3}{2} \frac{4k_w}{n\pi} \frac{NI}{2P} \sin(nP\theta_m \mp \omega t) \quad (36)$$

where

- sign holds for $n = 1, 7, 13, \dots$
- + sign holds for $n = 5, 11, 17, \dots$
- All other terms are zero

2.5. Torque Calculation

If the magnetic field energy is treated as stored in the air gap and the permanent magnet, the torque can be written as [1]

$$T = \frac{p\lambda l}{\pi} \int_0^{2\pi} \left\{ \frac{\partial}{\partial \theta_r} \left(\frac{1}{2}BF \right) \right\} d\theta_m = \frac{p\lambda l}{\pi} \int_0^{2\pi} \left\{ P(F_{3ph} + F_{RM}) \frac{\partial F_{RM}}{\partial \theta_r} \right\} d\theta_m \quad (37)$$

where p denotes the winding pole pairs, λ the winding-pole pitch, l the stack length of steel, B the flux density, P the permeance coefficient, and F the magnetomotive force.

3. SIMULATION RESULTS

Figure 10 shows the geometry of the current stator design, where the red color represents one of the eighteen movable stators while the gray color represents the fixed stator. The movable stator can be rotated from the leftmost position of 2.3 deg to the rightmost position of 19.9 deg. The calculation result of (3) by using MATLAB is shown in Figure 11, where the distance between PM and the stator base is 62.2 mm. A red line denotes the PM height measured from the stator base, and blue lines account for the fixed stator geometry.

This study designs the motor such that the motor structure is periodic, since every two stator slots become one set. Figure 12 depicts such a set of stator slots that is marked by AA' curve, starting from A to A' . Figure 13 compares computational results of magnetic flux in the motor between two positions of movable stators by using the finite element method, where current in and out of phases U , V , and W windings are also marked. There are nine stator slots, and each stator slot has a movable stator between two fixed stator teeth. Each phase on generates 5A current input in stator slots. Figures 13(a) and 13(c) show that flux line distributions vary with movable stator positions in slots. Figures 13(b) and 13(d) compare their flux density distributions. Note that flux lines pass through movable stators at any movable stator position. Hence, the flux density distribution and flux lines vary with movable stator positions, thereby varying the motor torque based on movable stator positions.

Figure 16 compares flux density distribution vs. θ_m between computational results by executing ANSYS Maxwell and analytical results by calculating (19). The flux density depicted in Figure 16 exhibits three peaks from 0 to 25 deg in both numerical and analytical results. The horizontal coordinates of three peaks respectively correspond to mechanical angles θ_m of a fixed stator teeth, a movable stator, and a fixed stator teeth. The first peak in Figure 16 results from a smaller air gap between the fixed

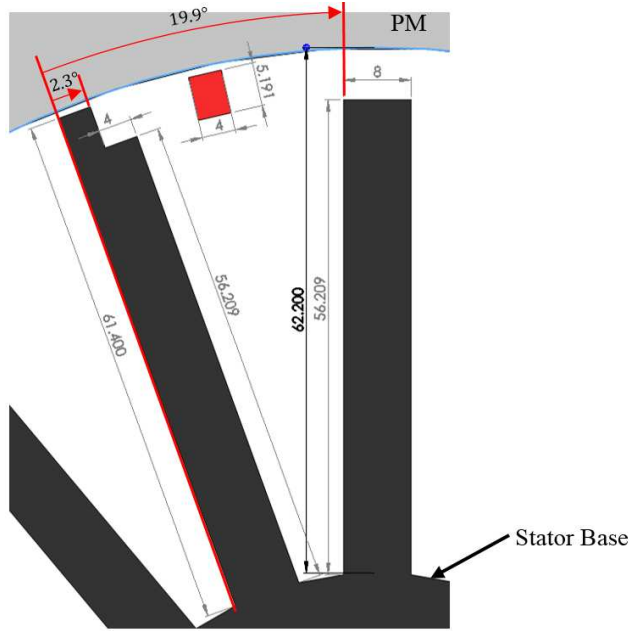


Figure 10. Geometry and dimension of the present stator that consists of movable stators in red color and the fixed stator in gray pattern (unit: mm).

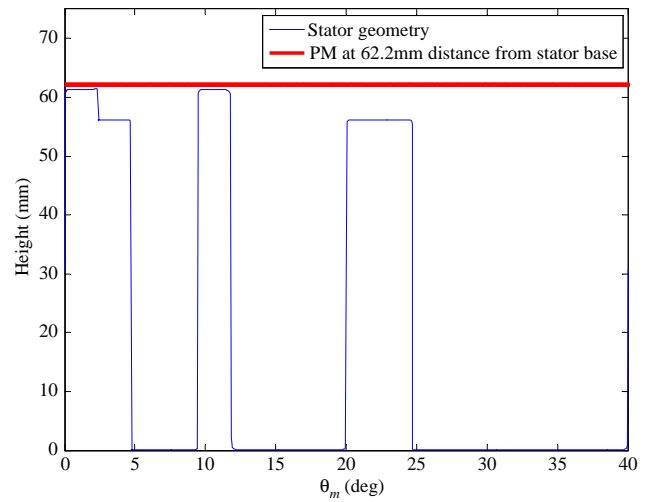


Figure 11. Diagram of the fixed stator drawn based on analytical solution.

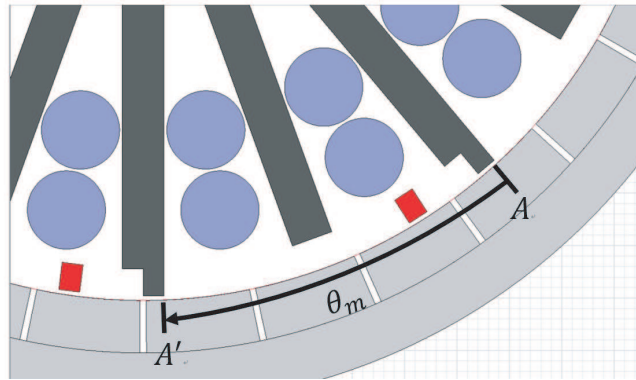


Figure 12. One set of stator teeth within AA' arc with a rectangular movable stator. θ_m corresponds to the horizontal axis in Figure 11.

stator and permanent magnet, according to Figure 10. Similarly, the second peak in Figure 16 results from another smaller air gap between the movable stator and permanent magnet. Figure 16 depicts that numerical and analytical results are consistent. Thus, the present analytical model indeed can be used to predict magnetomotive force generated from PM. Table 1 lists the motor dimensions and specifications in this study.

Figure 14 shows cogging torque numerical results when movable stator position is at 9.3 and 14.3 deg position measured according to Figure 12. According to the proposed motor design (18-slot 30-pole), the cycles per mechanical revolution [17] of cogging torque components are 90. In order to observe easily, the cogging torque numerical results are shown from 0 to 120 mechanical angle. Hence, one-third of the CPMR can be observed in both Figures 14(a) and 14(b).

Back-EMF waveforms are shown in Figure 15, and both movable stator positions are sinusoidal waves. The back-EMF waveform is in red dotted line when the movable stator is at 14.3 deg position

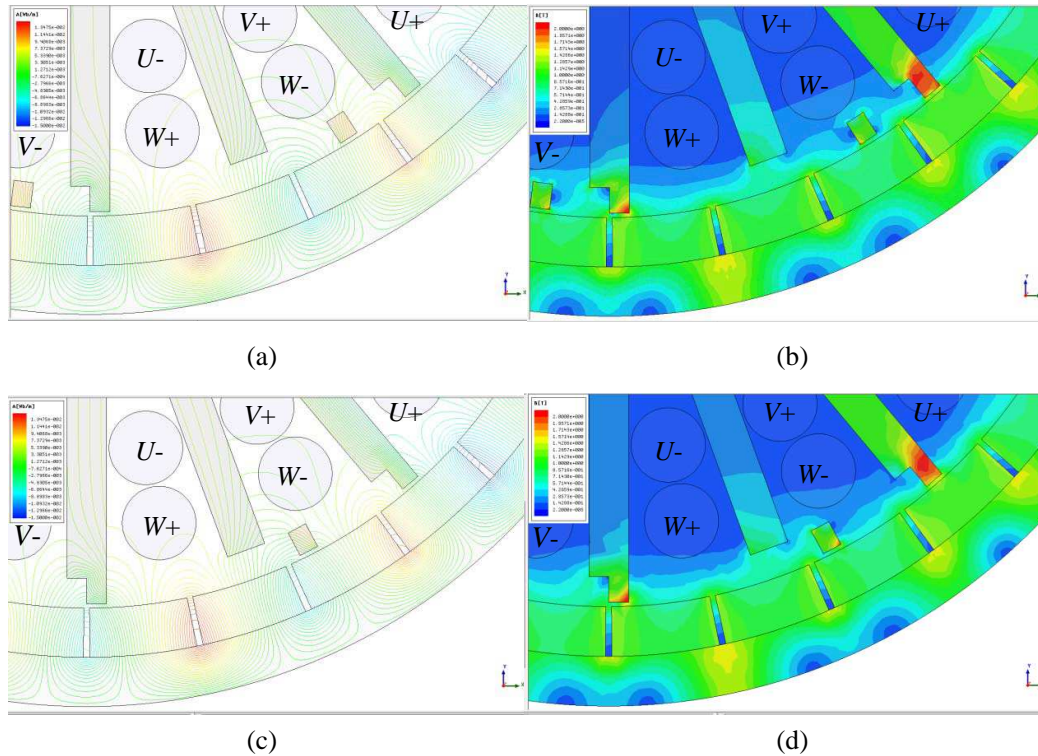


Figure 13. Computational results by using ANSYS Maxwell software with phases U , V , and W windings. (a) Flux distribution when the movable stator is at 9.3 deg position measured according to Figure 12. (b) Flux density when the movable stator is at 9.3 deg position measured according to Figure 12. (c) Flux distribution when the movable stator is at 14.3 deg position measured according to Figure 12. (d) Flux density when the movable stator is at 14.3 deg position measured according to Figure 12.

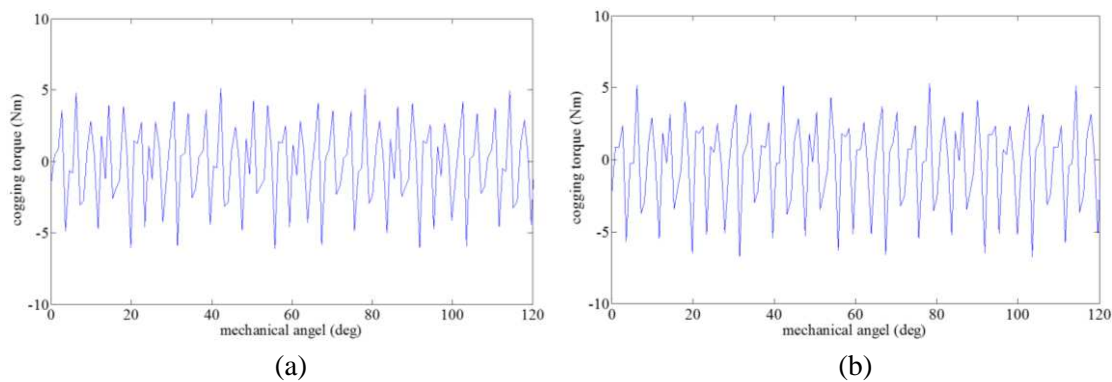


Figure 14. (a) Cogging torque when the movable stator is at 9.3 deg position measured according to Figure 10. (b) Cogging torque when the movable stator is at 14.3 deg position measured according to Figure 10.

with blue line when the movable stator is at 9.3 deg position. Obviously, the red dotted line is higher than the blue line, which means that different movable stator positions can generate different back-EMF waveforms.

For the use of electric vehicles, rotating the movable stator in this study will either manually or automatically change the motor torque. Figure 17 compares torque variations with the rotation angle

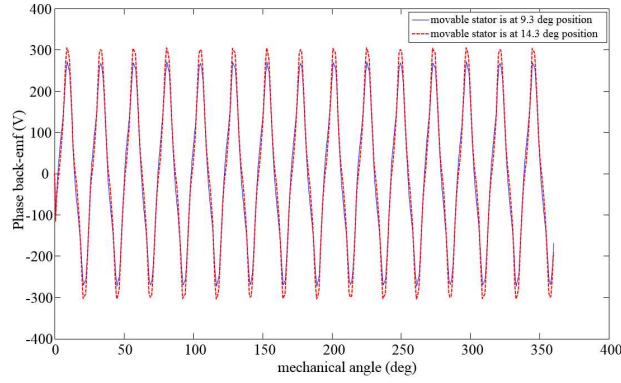


Figure 15. Phase back-EMF comparison between movable stator is at 9.3 and 14.3 deg position.

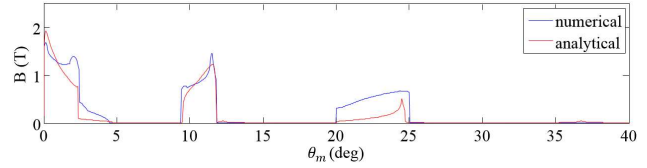


Figure 16. Flux density comparison within AA' slots between numerical and analytical results.

Table 1. Specifications prescribed in this study.

Parameter	Value	Unit
Geometrical Motor Characteristic		
Number of Slots	18	-
Pole Pitch	12	deg
Rotor Outer Diameter	241	mm
Stack Length	60	mm
Slot Depth	61.4	mm
Stator Teeth Width	8	mm
Movable Stator Width	4	mm
Movable Stator Depth	5.2	mm
Air-gap Length	0.8	mm
Winding Type	Concentrated	-
Number of Poles	30	-
Number of Turns of Coil per Pole	120	-
Speed	750	rpm
Number of Movable stators	9	-
Number of Fixed stator teeth	18	-
Supply Condition		
Current	5	A
Number of Phases	3	-
Drive Frequency	187.5	Hz
Material		
Silicon Steel	DW465-50	-
Permanent Magnet	NdFeB	-

between numerical and analytical results. The numerical results are calculated by the ANSYS Maxwell software, and the analytical results are calculated by using (37). The designed dimensions are listed in Table 1. As shown in Figure 17, the numerical and analytical results match well from 6.3 to 16.3 deg rotation angle of the movable stator. The 2.3 and 19.9 deg of moving angles of the movable stator represent the leftmost and rightmost movable stator positions, respectively. The analytical results

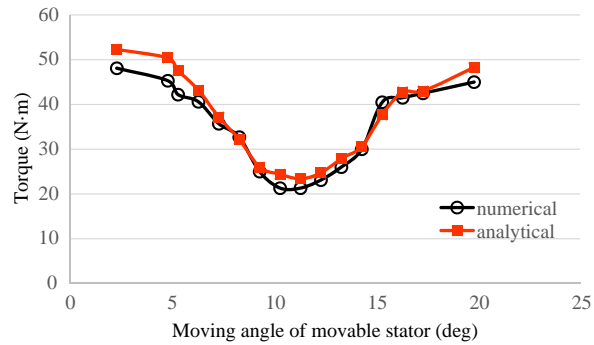


Figure 17. Comparison between numerical and analytical results in torque variation with stator moving angle.

are higher than numerical ones when the movable stator is moved to either the leftmost or rightmost position. This is caused by magnetic saturation that is not taken into account in analytical models.

4. CONCLUSION

This paper has presented an innovative permanent-magnet motor with movable stators. The flux density distribution and flux lines vary with movable stator positions, thereby varying the motor torque based on movable stator positions. The analytical model of movable stators has been established and validated by using the ANSYS Maxwell software. 2-D numerical results are generated and compared with analytical results. The torque of permanent-magnet motors can be varied by moving the movable stators, according to both numerical and analytical results. Concerning motor torque variation capability achieved in this study, according to Figure 15, the ratio of the largest vs. the smallest torque is calculated as $53/23 = 2.3$. In comparison, the 1st, 2nd, and 3rd gear ratios of traditional transmission in gasoline sedans such as VW Golf are 3.9, 3.45, and 1.9, respectively. Although the traditional transmission in gasoline sedans still has advantages in torque ratios, the weight and volume of transmissions increase fuel consumption of gasoline sedans. By contrast, the permanent magnet motor with movable stators proposed in this study is effective and promising in direct drive systems.

ACKNOWLEDGMENT

This work was supported by Industrial Technology of Research Institute, Taiwan, R.O.C.

REFERENCES

1. Toba, A. and A. T. Lipo, "Generic torque-maximizing design methodology of surface permanent-magnet vernier machine," *IEEE Transactions on Industry Applications*, Vol. 31, No. 6, 1539–1546, 2000.
2. Ishizaki, A., T. Tanaka, K. Takasaki, and S. Nishikata, "Theory and optimum design of PM vernier motor," *Seventh International Conference on Electrical Machines and Drives, (Conf. Publ. No. 412)*, 208–212, 1995.
3. Toba, A. and A. T. Lipo, "Novel dual-excitation permanent magnet vernier machine," *Industry Applications Conference*, Vol. 4, 2539–2544, 1999.
4. Tasaki, Y., Y. Kashitani, R. Hosoya, and S. Shimomura, "Design of the vernier machine with permanent magnets on both stator and rotor side," *Power Electronics and Motion Control Conference*, Vol. 1, 302–309, 2012.
5. Ho, S. L., S. Niu, and W. N. Fu, "Design of the vernier machine with permanent magnets on both stator and rotor side," *IEEE Transactions on Magnetics*, Vol. 47, No. 10, 3280–3283, 2011.

6. VuXuan, H., D. Lahaye, S. O. Ani, H. Polinder, and J. A. Ferreira, "Effect of design parameters on electromagnetic torque of PM machines with concentrated windings using nonlinear dynamic FEM," *IEEE International Electric Machine & Drives Conference*, 383–388, 2011.
7. Sanada, M., K. Ito, and S. Morimoto, "Equivalent air gap shortening by three-dimensional gap structure for torque improvement of electric machines," *Electrical Machines and Systems Conference*, 1–6, 2009.
8. Zhang, Y., L. Jing C. Li, G. Tu, and J. Jiang, "Semi-analytical method for air gap main magnetic field computation of direct drive permanent magnet torque motors," *Electrical Machines and Systems Conference*, 1–4, 2011.
9. Kano, Y. and N. Matsui, "A design approach for direct-drive permanent-magnet motors," *IEEE Transactions on Industry Application*, Vol. 44, No. 2, 1–4, 2008.
10. Chau, K. T., D. Zhang, J. Z. Jiang, C. Liu, and Y. Zhang, "Design of a magnetic-g geared outer-rotor permanent-magnet brushless motor for electric vehicles," *IEEE Transactions on Magnetics*, Vol. 43, No. 6, 2504–2506, 2007.
11. Chen, G. H. and K. J. Tseng, "Design of a permanent-magnet direct-driven wheel motor drive for electric vehicle," *Power Electronics Specialists Conference*, Vol. 2, 1933–1939, 1996.
12. Zhao, W., M. Cheng, and R. Cao, "Electromagnetic analysis of a modular flux-switching permanent-magnet motor using finite-element method," *Progress In Electromagnetics Research B*, Vol. 43, 239–253, 2012.
13. Boughrara, K., T. Lubin, R. Ibtouen, and M. N. Benallal, "Analytical calculation of parallel double excitation and spoke-type permanent-magnet motors; simplified versus exact model," *Progress In Electromagnetics Research B*, Vol. 47, 145–178, 2013.
14. Mahmoudi, A., N. A. Rahim, and H. W. Ping, "Genetic algorithm and finite element analysis for optimum design of slotted torus axial-flux permanent-magnet brushless DC motor," *Progress In Electromagnetics Research B*, Vol. 33, 383–407, 2011.
15. Gao, J., L. Zhang, and X. Wang, *AC Machine Systems*, Springer-Verlag, Berlin, 2009.
16. Fitzgerald, A. E., C. Kingsley, Jr., and S. D. Umans, *Electric Machinery*, McGraw-Hill, Singapore, 1983.
17. Islam, M. S., S. Mir, and T. Sebastain, "Issues in reducing the cogging torque of mass-produced permanent-magnet brushless DC motor," *IEEE Transactions on Industry Applications*, Vol. 40, No. 3, 813–820, 2004.